Advances in Water Resources 145 (2020) 103741

Contents lists available at ScienceDirect

Advances in Water Resources

journal homepage: www.elsevier.com/locate/advwatres

Pore-network modeling of single-phase reactive transport and dissolution pattern evaluation

Barbara F. Esteves[a,b], Paulo L.C. Lage[a], Paulo Couto[c], Anthony R. Kovscek[b,*]

[a] Universidade Federal do Rio de Janeiro, Chemical Engineering Department (PEQ/COPPE), Rio de Janeiro, RJ, 21941-972, Brazil
[b] Stanford University, Energy Resources Engineering, Stanford, CA 94305, USA
[c] Universidade Federal do Rio de Janeiro, Civil Engineering Department (PEC/COPPE), Rio de Janeiro, RJ, 21941-972, Brazil

ARTICLE INFO

Keywords:
Pore network modeling
Reactive transport
Dissolution pattern
Pore-scale modeling

ABSTRACT

A pore-network modeling approach is proposed to understand mineral dissolution regimes during reactive transport, as well as changes in porosity and permeability. The transport problem is implemented with full consideration of the mass balance of the solute in all pore spaces, including pore-bodies and throats. The changes in geometry of the pore network due to calcite dissolution are taken into account based on the rate of the heterogeneous chemical reaction happening at the mineral surface. The networks consider two- and three-dimensional domains with a variety of number of pores. The evolution of network geometry and flow properties are investigated under various flow conditions using representative Péclet and Damköhler numbers to understand the interplay of transport and reaction. A behavior diagram is constructed aiming to identify different regimes and their boundaries. The dissolution patterns identified in this study further the applicability of the pore-network model approach as a tool for understanding of reactive transport and dissolution processes.

1. Introduction

Reactive transport in porous media and mineral dissolution processes are of extreme interest for many subsurface applications, including CO_2 storage, Enhanced Oil Recovery (EOR), and acidizing for stimulation (Sohrabi et al., 2012; Wolterbeek and Raoof, 2018; Menke et al., 2018; Gharbi et al., 2013). Changes in porosity and permeability of porous media, as well as the observation of various dissolution patterns of the porous medium are consequences of these dynamic processes (Algive et al., 2010; Soulaine et al., 2017).

Depending on the dominant transport mechanism and the reactivity of the mineral solid surface, different dissolution patterns through a porous medium can be observed (Golfier et al., 2002; Soulaine et al., 2017). Consequently, good understanding of the dissolution processes is imperative to assess long-term reservoir integrity properties for CO_2 storage and to design efficiently acidizing treatments (Rathnaweera et al., 2016; Bemer and Lombard, 2010; Fredd and Dowell, 2000).

With respect to CO_2 injection for storage and for EOR, rock mechanical changes may be induced by chemical reactions, especially in porous media with substantial carbonate minerals (Egermann et al., 2010; Rathnaweera et al., 2016; Bemer and Lombard, 2010). For geological CO_2 storage such mineralogical alterations may be of concern for the safety and efficiency of the technique because mineral dissolution may increase the chance for leakage and also CO_2 migration out of the storage formation (Egermann et al., 2010; Rathnaweera et al., 2016; Bemer and Lombard, 2010). As discussed by Ott and Oedai (2015), the consequences of these dynamics interactions are dependent on the transport regimes. Formation of preferential pathways bypasses rock matrix and leads to poor utilization of the pore space for the storage of CO_2; surface dissolution alters the mechanical integrity of the rock near the well, where most of the acid is consumed; and uniform dissolution might lead to subsidence due to weakening of mechanical properties of the reservoir.

Regarding acidizing for well stimulation, formation of preferential pathways increases the overall conductance through the reservoir and, consequently, the well productivity (Hill and Schechter, 2000; Ott and Oedai, 2015). Also, for a given volume of injected fluid, the deeper the wormhole penetration into the reservoir the better. Therefore, single dominant wormhole channels at intermediate injection rates are often desired and represent the most effective stimulation (Fredd and Fogler, 1999).

In this context, dimensionless numbers characterize reactive-transport regimes (Steefel and Mäher, 2009). The use of dimensional analysis is a standard tool in fluid mechanics that aims to derive the relevant dimensionless parameters that control the physics of a specific problem (Békri et al., 1995). The Péclet number (*Pe*) is defined as the ratio of the advection rate to the rate of diffusion of a chemical species and the Damköhler number (*Da*) is defined as the ratio of the reaction

* Corresponding author.
E-mail addresses: besteves@stanford.edu (B.F. Esteves), kovscek@stanford.edu (A.R. Kovscek).

https://doi.org/10.1016/j.advwatres.2020.103741
Received 31 January 2020; Received in revised form 28 July 2020; Accepted 21 August 2020
Available online 22 August 2020

Nomenclature

z	Coordination number
q_{ij}	Volumetric flow rate through throat ij
c_{ij}	Conductance of throat ij
P_i	Pressure in pore i
P_j	Pressure in pore j
r_{ij}	Cross-section radius of the throat ij
μ	Dynamic viscosity of the fluid
l_{ij}	Length of the throat ij
K	Absolute permeability of the network
ΔP	Pressure difference through the network
A	Cross-sectional area of the network
L	Length of the network
t	Time
$c_{\alpha,i}$	Mass concentration of species α in pore i
$c_{\alpha,ij}$	Mass concentration of species α in throat ij
V_i	Volume of pore i
D_α	Diffusion coefficient of species α
r_i	Radius of pore i
$R_{(het)\alpha}$	Reaction rate of specie α due to heterogeneous chemical reaction
$A_{r,i}$	Available reactive surface area of pore i
$c_{\alpha,in}$	Mass concentration of specie α in the pore from where the flow is arriving in the throat ij
$A_{r,ij}$	Available reactive surface area of throat ij
A_r	Available reactive surface area of the pore space
β	Stoichiometric coefficient that relates the consumed species α with the consumed reactive mineral
ρ_{solid}	Density of the solid reactive mineral
k_r	Kinetic constant of the heterogeneous chemical reaction
c_A	Acid mass concentration of the pore or throat
$R_{(het)A}$	Reaction rate of acid due to heterogeneous chemical reaction
$m_{A,con}$	Consumed mass of acid
$m_{solid,con}$	Consumed mass of solid
V_{con}	Consumed volume
dV_i	Volume change in pore i
dV_{ij}	Volume change in throat ij
dr_i	Radius change in pore i
dr_{ij}	Radius change in throat ij
$dV_{i,ij}$	Volume doubly dissolved by throat ij and the connected pore i
$dV_{j,ij}$	Volume doubly dissolved by throat ij and the connected pore j
$A_{i,ij}$	Surface area of the semi-sphere formed by pore i and throat ij
Re	Reynolds number
ρ_f	Fluid density
v_0	Characteristic velocity represented here by the inlet velocity
$PeDa$	Péclet-Damköhler number
A_{ss}	Specific surface area of the porous medium
Da	Damköhler number
σ	The standard deviation of the logarithmic of the acid concentration
$\frac{N}{\log_{10} c_{A,x}}$	Number of pores and throats that are evaluated Mean value of the logarithmic of acid concentration of all data set

rate to the advection rate. The Péclet-Damköhler number (*PeDa*) is the ratio of the reaction rate and the diffusive mass transfer rate.

Based on dimensionless numbers, behavior diagrams (or phase diagrams) are useful to define flow boundaries for different dissolution regimes (Daccord et al., 1993b; Golfier et al., 2002; Soulaine et al., 2017; Liu and Mostaghimi, 2017; Song et al., 2018). Porosity-permeability relationships have also been used to understand and characterize different patterns of dissolution in porous media at the pore-scale (Békri et al., 1995; Algive et al., 2010; Liu and Mostaghimi, 2017; Soulaine et al., 2017).

Uniform dissolution is described as a reaction-limited process, where the reactive solute is spread over the whole porous medium and the dissolution is nearly uniform all-over the available reactive surface (Békri et al., 1995; Golfier et al., 2002). This regime is defined by Békri et al. (1995) for $PeDa < 1$ and by Soulaine et al. (2017) for $Da \leq 1$, while for Liu and Mostaghimi (2017) the boundaries of this regime depend on the correlation length of the porous medium. Note that characteristic lengths used to compute the dimensionless numbers are not the same, and consequently, boundaries between the different regimes are different, despite the agreement of the general features of the behavior diagrams.

For systems with greater reactivity, in the case of Békri et al. (1995) for $PeDa > 1$, the dissolution pattern depends upon the dominant transport process. Surface dissolution (or compact dissolution) is characterized by the domination of the diffusion mechanism over transport by advection and, consequently, dissolution mainly occurs in the inlet area of the porous medium (Liu and Mostaghimi, 2017; Golfier et al., 2002). In this regime a uniform concentration profile is observed along the cross-sections perpendicular to the flow. Soulaine et al. (2017) observed this pattern for $Pe \leq 10^{-2}$ and $Da > 1$. Preferential pathways (or wormholing) are observed when the predominant mechanism is advection. For Békri et al. (1995) this regime is observed for $PeDa > 1$ and for Soulaine et al. (2017) for $Da > 1$. A mixed dissolution pattern is described by Liu and Mostaghimi (2017) as a transition zone between face dissolution and wormholing.

Soulaine et al. (2017) and Golfier et al. (2002) differentiate wormholing using three different regimes. Conical wormholes are observed for larger injection rates, but still in a diffusion-dominated mechanism, where solute starts to penetrate into the porous medium and the uniform patterns along the vertical cross-sections are no longer observed ($10^{-2} < Pe \leqslant 1$ and $Da > 1$ for Soulaine et al. (2017) and around $10^{-3} < Pe < 10^{-2}$ and $Da > 10^{-3}$ for Golfier et al. (2002)). One dominant wormhole can be observed for intermediate flow rates ($1 < Pe \leq 10$ and $Da > 1$, according to Soulaine et al. (2017)) where the reactive solute penetrates preferentially into the biggest pore spaces to form flow channels and, consequently, the formation of a dominant wormhole. Ramified wormholes occur at large injection rates, for $Pe > 10$ and $Da > 1$ (Soulaine et al., 2017), and are characterized by wormholes becoming more branched.

In order to investigate the dissolution processes in porous media, several numerical approaches and experiments have been developed. Numerical schemes based on random walks and finite difference formulations were used by Békri et al. (1995) to explore the effects of dissolution on different porous media configurations. Liu and Mostaghimi (2017) proposed a lattice Boltzmann method to explore the effects of different correlation lengths on dissolution patterns. Soulaine et al. (2017) proposed a micro-continuum Darcy-Brinkman-Stokes (DBS) approach, which considers Stokes flow in the void areas and Darcy's law for transport through the matrix, that was also compared with micromodel experiments simulating the dissolution of a calcite grain. Golfier et al. (2002) used a three-dimensional coupled reaction transport Darcy-scale model that was directly compared with dissolution experiments performed on two-dimensional beds of packed grains of salt, reflecting dissolution processes occurring during acid injection in limestone.

Pore network modeling is another numerical approach that has been used to study reactive flow and dissolution processes. Hoefner and Fogler (1988) pioneered the use of pore network modeling to study

dissolution of porous media and to evaluate qualitatively the formation of wormhole channels based on the Damköhler number. Fredd and Fogler (1998) went beyond and combined effects of transport and reaction to predict wormhole structure by using two-dimensional networks and also a three-dimensional physically representative network based on packed-bed representation of the porous medium. Note that in both studies, mixing occurs only in the pores and only throats are allowed to grow due to dissolution.

More recently, Algive et al. (2007, 2010) and Bekri et al. (2015) used pore-network models to investigate changes in petrophysical properties in the presence of reactive fluid based on permeability-porosity relationships for different flow conditions and also investigated different dissolution regimes for the case of deposition in porous media. The approach of their studies considers that the system is not very far from chemical equilibrium and that the asymptotic regime has been reached. In this way, the solute concentration undergoes an exponential evolution with time and moment theory is applied to determine the macroscopic transport coefficients of the transport equation. Tansey and Balhoff (2016) studied dissolution of a porous medium due to a reactive single-phase transport in the mass-transfer-limited regime also using pore-network modeling. Simulations were conducted on random close-pack arrangements of spheres, where the mass balance equation was solved for pore-bodies only and no phase diagram was explored.

Pore network modeling is a technique that is widely used to represent natural porous media where complex pore geometries are represented using a simplified pore-and-throat type network Algive et al. (2010). Since the pioneering work of Fatt (1956), that studied two-phase flow and capillary pressure curves, pore-network models have been successfully applied in numerous research areas, including reactive transport and dissolution problems (Li et al., 2006; Algive et al., 2010; Raoof et al., 2012). The computational efficiency of pore-network models are related to the simplicity of their geometry and because of this feature, pore-network modeling is considered applicable to much larger domains when compared to direct simulation methods (Mehmani and Balhoff, 2015; Yang et al., 2016).

The main objective of this study is to understand the occurrence of different dissolution regimes in a porous medium subject to various reactive flow conditions during single-phase flow relevant to geological sequestration of CO_2 using the pore-network modeling approach. Modeling of the pore-scale phenomena involved in reactive flow through porous media is an important step towards understanding the changes in permeability and porosity as well as different dissolution patterns observed at larger scales.

The main contribution of this work is to identify different dissolution regimes in a phase-diagram format, based on dimensionless numbers, using a complete pore network model that takes into account species mass balance inside pore and throat volumes, as well as the evolution of pore-space geometry and network flow field during reactive transport simulations. Qualitative criteria are often used to evaluate different dissolution patterns, including evolution of acid concentration, network geometry, fluid volumetric flow rate and porosity-permeability relationship. Here, a quantitative criterion based on standard deviation analysis is introduced to classify the regime by interpreting acid distribution within pore space.

In the remainder of the paper, we first present the governing equations of the pore-network model that simulates reactive transport and dissolution, as well as the computational implementation of these equations and the pore-networks selected for this study. Finally, we present the simulation results and discuss the regimes observed. We close with a summary and conclusions.

2. Pore network models construction

Porous media are investigated using two- and three-dimensional (2D and 3D) cubic pore-network models. The pores are characterized as spherical and are connected to each other by cylindrical throats with circular cross-sections. The size of the pores respect a uniform distribution and the size of the throats are related to the size of the pores connected to them. Throat diameters were defined as 1/4 of the diameter of the smallest pore connected to a throat and interpore distances are equal. Pore walls are assumed to be composed of a single mineral such as calcite.

A more complex network derived from a real carbonate rock sample is also presented. This pore network is generated from micro-computed tomography (micro-CT) and was obtained from a data set made available by Imperial College London in *Statoil* format (PERM, 2020).

Pore networks were constructed using OpenPNM, which is an open-source pore-network modeling package that is designed to be customized. Users can write their own pore-scale models or even use or edit some of the available routines (Gostick et al., 2016). Another feature of OpenPNM is the possibility to generate cubic and random networks, in the most varied pore and throat size distributions. It is also possible to import networks from different formats.

3. Governing equations

The governing equations of the reactive transport problem with dissolution of the porous medium are presented in this section, as follows: pressure field determination, mass balance, simplified kinetic approach, the geometry update, standard deviation criterion for interpreting acid distribution, and dimensionless numbers.

3.1. Steady-state flow field

In order to obtain the pressure field of the network, we consider the steady-state flow of a single-phase incompressible fluid, in which the mass conservation for each pore is given by

$$\sum_{ij}^{z} q_{ij} = 0, \tag{1}$$

where z is the coordination number and q_{ij} is the volumetric flow rate through throat ij. The volumetric flow rate through a pore-throat is determined by the pressure difference between the connected pores i and j $(P_i - P_j)$ and the throat conductance (c_{ij}), as follows:

$$q_{ij} = c_{ij}\left(P_i - P_j\right). \tag{2}$$

The throat conductance is obtained by use of Poiseuille's law for laminar flow in a cylindrical tube:

$$c_{ij} = \frac{\pi r_{ij}^4}{8\mu l_{ij}}, \tag{3}$$

where r_{ij} is the radius of throat ij cross-section, μ is the dynamic viscosity of the fluid and l_{ij} is the length of the throat ij. Substituting Eqs. (2) and (3) into Eq. (1), a linear algebraic system for the unknown pressure field is solved for the pressure in each pore.

To determine the steady-state flow field of the network, constant volumetric flow rate at the inlet boundary and fixed pressure at the outlet boundary are imposed. Also, to determine the absolute permeability, fixed pressures are imposed at the inlet and outlet boundaries. Both systems result in a one-dimensional flow problem. Considering the last case, the total flow rate through the network (Q) is obtained after pressure field determination and Darcy's law is used to calculate the absolute permeability (K) of the system, as described below

$$K = \frac{\mu Q L}{A \Delta P}, \tag{4}$$

where A is the cross-sectional area of the network and L is the length of the network.

3.2. Concentration field

The reactive transport and dissolution problem is described by the mass balance in all available pore spaces, pores, and throats, and is deduced from the mass conservation equations of the chemical species

(Bird et al., 2011). The transport of a chemical species occurs by advection and diffusion. For a control volume represented by pores, the mass balance equation for chemical species α in pore i is

$$\frac{d}{dt}(c_{\alpha,i}V_i) = \sum_{ij,in} c_{\alpha,ij}q_{ij} - c_{\alpha,i}\sum_{ij,out} q_{ij} + \sum_{ij} A_{ij}\mathcal{D}_\alpha\left(\frac{c_{\alpha,ij}-c_{\alpha,i}}{0.5l_{ij}+r_i}\right) - R_{(het)\alpha}A_{r,i}, \tag{5}$$

where t is the time, $c_{\alpha,i}$ is the mass concentration of species α in pore i, $c_{\alpha,ij}$ is the mass concentration of species α in throat ij, V_i is the volume of pore i, A_{ij} is the cross-sectional area of throat ij, $\mathcal{D}_\alpha$ is the diffusion coefficient of species α, r_i is the radius of pore i, $R_{(het)\alpha}$ is the reaction rate of species α due to heterogeneous chemical reaction and $A_{r,i}$ is the available reactive surface area of pore i. On the left-hand side is the accumulation term, that is discretized later in this section. On the right-hand side, the first two terms take into account advective mass inflow rates, represented by the mass that arrives in pore i from connected throats ij, and advective mass outflow rate, represented by the mass that leaves pore i through throats ij; the third term describes the mass change rate due to diffusion between pore i and all connected throats ij; and the last term describes the mass change of species α due to heterogeneous chemical reaction that occurs in the available reactive surface area of pore i.

For control volumes represented by throats, the mass balance equation for species α in throat ij is

$$\frac{d}{dt}(c_{\alpha,ij}V_{ij}) = (c_{\alpha,in}-c_{\alpha,ij})q_{ij} + A_{ij}\mathcal{D}_\alpha\left(\frac{c_{\alpha,i}-c_{\alpha,ij}}{0.5l_{ij}+r_i}\right) + A_{ij}\mathcal{D}_\alpha\left(\frac{c_{\alpha,j}-c_{\alpha,ij}}{0.5l_{ij}+r_j}\right) - R_{(het)\alpha}A_{r,ij}, \tag{6}$$

where $c_{\alpha,in}$ is the mass concentration of species α in the pore from where the flow is arriving in the throat ij and $A_{r,ij}$ is the reactive surface area of throat ij. On the right-hand side of Eq. (6), the first term takes into account the mass change due to advection between the inlet and the outlet zones of throat ij, that are described by the mass of species α that arrives in throat ij from the connected pore i or j, depending on the flow direction. The inflow concentration is represented by $c_{\alpha,in}$, and the mass of α that leaves throat ij in the direction of the other connected pore is $c_{\alpha,ij}$. The second and third terms represent the mass change rate by diffusion phenomena between the throat ij and the connected pores i and j, respectively. The last term presents the mass change of species α due to heterogeneous chemical reaction that occurs in the available reactive surface area of throat ij.

The Euler implicit method is used to discretize the time derivatives in Eqs. (5) and (6), and to set up the linear system for the unknown concentration of α species in all pores and throats of the network at each time step. The linear system is solved by using a direct method from the SciPy library (Jones et al., 2001).

The domain initial condition and the inlet boundary condition are represented by a fixed value of species concentration, as presented below, respectively:

$$c_{\alpha,i}\,|_{t=0} \; and \; c_{\alpha,ij}\,|_{t=0} = c_{\alpha,0} = constant, \tag{7}$$

$$c_{\alpha,inlet}\,|_{\forall t} = c_{\alpha,I} = constant, \tag{8}$$

where $c_{\alpha,intlet}$ is the acid mass concentration in the inlet pore spaces. The boundary condition at outlet pores are represented by a sink term, where the mass of acid that arrives at outlet pores by advection phenomenon, from all connected throats, will leave these pores with the same total volumetric flow rate that arrives in each of these pores ($q_{i,sink}$), as follows

$$c_{\alpha,i,outlet}q_{i,sink}\,|_{\forall t} = \sum_{ij,in} c_{\alpha,ij}q_{ij}, \tag{9}$$

where $c_{\alpha,i,outlet}$ is the acid mass concentration in the outlet pore i.

Finally, discretization of the accumulation term of mass balance equations is expressed by the product rule. In our approach, the concentration field is solved implicitly and the volume explicitly. In other words, the system is solved for the new concentrations based on the previous geometry, and then, geometry is updated, as indicated by:

$$\frac{d}{dt}(c_\alpha V) = V\frac{dc_\alpha}{dt} + c_\alpha\frac{dV}{dt} = V^n\frac{c_\alpha^{n+1}-c_\alpha^n}{\Delta t} + c_\alpha^{n+1}\frac{V^n-V^{n-1}}{\Delta t}, \tag{10}$$

where V represents the volume of both pores and throats, and the superscripts n, $n+1$ and $n-1$ represent, respectively, the present, the next, and the previous instants.

3.3. Dissolution reactions

During the dissolution process, porous medium geometry evolves with heterogeneous chemical reactions at the available reactive surfaces of pores and throats.

For simplicity, reactive surfaces are represented by the presence of only one mineral, that is dissolved by the presence of an acid species. This approach represents, in a simplified way, the acidization processes where hydrochloric acid (HCl) is injected in carbonate rocks, represented by calcite ($CaCO_3$), as follows

$$CaCO_{3(s)} + 2HCl_{(aq)} \rightarrow CaCl_{2(aq)} + CO_{2(aq)} + H_2O_{(l)}. \tag{11}$$

Because the acid is the only component in the aqueous phase that reacts with the solid mineral, it is the only chemical species concentration that needs to be tracked. The other species are determined by stoichiometry. Note that the rate-limiting reaction is the acid attack on calcite, and it is assumed that carbonate equilibria is totally shifted toward $CO_{2(aq)}$ due to the high acid concentration in the system. Thus, a single reaction rate is sufficient to represent our problem. This approach follows from the work of Soulaine et al. (2017).

3.4. Geometry definitions and update

As our solution involves geometry changes, at each time step during the simulations, control volumes of pores and throats are changed. In this way, after each time step, with the solution of the concentration field based on mass balance, the change in volume of the pore spaces is obtained by the relation between the solid consumed on the available reactive surface of each pore space and the density of the reactive mineral that composes the porous medium. Considering a first-order reaction rate for the heterogeneous chemical reaction and a stoichiometric coefficient that relates the consumption of the hydrochloric acid ($\alpha = A$) and the consumption of the reactive mineral, the change in volume of the solid as a function of time is given by:

$$\frac{dV}{dt} = \frac{R_{(het)A}A_r\beta}{\rho_{solid}} = \frac{(k_r c_A)A_r\beta}{\rho_{solid}}, \tag{12}$$

where A_r is the available reactive surface area of the pore or throat, c_A is the acid mass concentration of the pore or throat, β is the stoichiometric coefficient that relates the acid consumption to the consumed reactive mineral, ρ_{solid} is the density of the solid reactive mineral and k_r is the kinetic constant of the heterogeneous chemical reaction. From Eq. (12), it is possible to identify three important quantities: consumed mass of acid ($m_{A,con}$), consumed mass of solid (m_{solid}) and consumed volume of solid (V_{con}), as presented below, respectively:

$$m_{A,con} = (k_r c_A)A_r\Delta t, \tag{13}$$

$$m_{solid,con} = \beta m_{A,con}, \tag{14}$$

$$V_{con} = \frac{m_{solid,con}}{\rho_{solid}}. \tag{15}$$

Based on the consumed volume, Eq. (15), it is possible to determine the change in volume of pores (dV_i) and throats (dV_{ij}), and relate these volume changes to the increase of pore radii (dr_i) and to the estimation of the increase of throat radii (dr_{ij}), as presented below:

$$dV_i = 4\pi r_i^2 dr_i, \tag{16}$$

$$dV_{ij} = 2\pi r_{ij} l_{ij} dr_{ij}. \tag{17}$$

At the junction of the throat with each pore, this procedure double counts the dissolution of the volumes presented below:

$$dV_{i,ij} = 2\pi r_{ij} dr_i dr_{ij}, \tag{18}$$

$$dV_{j,ij} = 2\pi r_{ij} dr_j dr_{ij}, \tag{19}$$

where $dV_{i,ij}$ and $dV_{j,ij}$ are the volumes doubly dissolved by throat ij and the connected pores i and j, respectively. Considering this information and the premise that double dissolution is maintained, the new pores and throats volumes are determined, respectively, by

$$V_i^{n+1} = V_i^n + dV_i + \sum_{ij} dV_{i,ij}, \tag{20}$$

$$V_{ij}^{n+1} = V_{ij}^n + dV_{ij} - dV_{i,ij} - dV_{j,ij}. \tag{21}$$

The pore volume is defined considering the volume of a sphere and, consequently, the updated radius of the pore is calculated as

$$V_i^{n+1} = \frac{4}{3}\pi \left(r_i^{n+1}\right)^3. \tag{22}$$

The change in pore radius, more precisely, the increase in pore radius as a consequence of the dissolution process, affects the length of the throats of the network because the pore volume invades part of the volume that previously belonged to the connected throats. The change in throat length caused by the changes in connected pores radii is given by

$$l_{ij}^{n+1} = d_{ij} - r_i^{n+1} - r_j^{n+1}, \tag{23}$$

where d_{ij} is the distance between the centers of two connected pores i and j. The volume of the throats are obtained considering the control volume as a cylinder. Given the updated throat length, it is possible to determine the throat radius, using Eq. (24)

$$V_{ij}^{n+1} = \pi \left(r_{ij}^{n+1}\right)^2 l_{ij}^{n+1}. \tag{24}$$

New throat available reactive area and cross-sectional area are obtained, respectively, by

$$A_{r,ij}^{n+1} = 2\pi r_{ij}^{n+1} l_{ij}^{n+1}, \tag{25}$$

$$A_{ij}^{n+1} = \pi \left(r_{ij}^{n+1}\right)^2. \tag{26}$$

Finally, considering the inlet and outlet areas of each pore defined by the sum of the spherical cap surfaces formed between the pore i and all connected throats ij (Eq. (27)), it is possible to determine the available reactive surface area of each pore, as presented below:

$$A_{i,ij}^{n+1} = 2\pi r_i^{n+1} \left(r_i^{n+1} - \sqrt{\left(r_i^{n+1}\right)^2 - \left(r_{ij}^{n+1}\right)^2} \right) \tag{27}$$

$$A_{r,i}^{n+1} = 4\pi \left(r_i^{n+1}\right)^2 - \sum_{ij} A_{i,ij}, \tag{28}$$

where $A_{i,ij}$ is the surface area of the semi-sphere formed by pore i and throat ij.

The above procedure is repeated for each time step and, because of this, it is possible to evaluate the evolution of the permeability and also the pore space during the simulation of the reactive transport coupled with dissolution process.

3.5. Dimensionless numbers

The use of dimensionless numbers in reactive transport aims to generalize predictions and results across a range of transport and reaction rate conditions. Problems involving reactive transport usually take into account Reynolds (Re), Péclet (Pe), Damköhler (Da) and Péclet-Damköhler ($PeDa$) numbers to characterize different dissolution patterns. The definitions used in this work are based on Soulaine et al. (2017) and calculated at the initial time. Reynolds number (Re) expresses the ratio of inertial effects to viscous forces and it determines the character of the flow (laminar, turbulent and transient flows) and is given by

$$Re = \frac{\rho_f v_0 \sqrt{K}}{\mu_f}, \tag{29}$$

where ρ_f is the fluid density, v_0 is a characteristic velocity represented here by the inlet velocity, $\sqrt{K}$ is the square root of the permeability of the porous medium and represents a characteristic length, and μ_f is the fluid dynamic viscosity. The Péclet number (Pe) is defined as the ratio of the advection rate to the rate of diffusion of a chemical species, as

$$Pe = \frac{v_0 \sqrt{K}}{D_\alpha}, \tag{30}$$

where D_α is the diffusion coefficient of species α. The Péclet-Damköhler ($PeDa$) is defined as the ratio of the reaction rate and the diffusive mass transfer rate, as

$$PeDa = \frac{k_r}{A_{ss} D_\alpha}, \tag{31}$$

where k_r is the constant of reaction and (A_{ss}) is the specific surface area of the porous medium, defined as the total available reactive surface area of the network divided by the total volume of pore spaces. Finally, the Damköhler number (Da), that represents the ratio of the reaction rate to the rate of advection, is defined as the ratio of the $PeDa$ and Pe numbers, as

$$Da = \frac{k_r}{v_0 \sqrt{K} A_{ss}}. \tag{32}$$

3.6. Statistics and regimes classification

Statistical approaches are useful for extracting information from a given data set and to better understand observed patterns. In this way, the standard deviation of the logarithm of the acid concentration (σ) is used in this study as a quantitative criterion to define dissolution regimes. This parameter is a measure of the spread of a set of values, hence, the smaller the deviation the more homogeneous is the data set. Based on numerous observations of simulation results in cubic networks, and for the initial condition used in these tests ($c_{a,0} = 10\ kg/m^3$), the limit σ value to categorize a normalized data set as homogeneous was observed to be 1.

Therefore, two different measures are considered: the standard deviation of the acid concentration over all pores and throats of the network (σ_{net}) and the average of the standard deviations of each vertical cross-section of the network ($\overline{\sigma_{cross}}$). First, σ_{net} is evaluated. If $\sigma_{net} < 1$ the acid concentration is considered uniform through the network and the regime is classified as uniform. Otherwise, the $\overline{\sigma_{cross}}$ is evaluated and if $\overline{\sigma_{cross}} < 1$ the acid concentration is considered to be uniform in each vertical cross-section of the network and the regime is classified as surface dissolution. Otherwise, the regime is classified as preferential pathways. The standard deviation criterion is obtained as

$$\sigma = \sqrt{\frac{1}{N} \sum_{x=1}^{N} \left(\log_{10} c_{A,x} - \overline{\log_{10} c_{A,x}} \right)^2}, \tag{33}$$

where N is the number of pores and throats that are evaluated and $\overline{\log_{10} c_{A,x}}$ is the mean value of the logarithm of acid concentration in the data set.

For the construction of the phase diagrams, the standard deviation analysis is evaluated for 100 random networks with the same size distribution and considering the same flow and reactive parameters. In this way, it is possible for each dissolution regime to present the number of networks that respected the criterion proposed to identify the main patterns.

4. Implementation

The base-algorithm from OpenPNM used for the implementation of the reactive transport and dissolution process was the *Transient Reactive Transport algorithm*, designed to account for advection, diffusion, and reaction phenomena considering just pores as control volumes and without considering geometry changes during simulations. In this way, the main improvements implemented by this work are related to considering pores and throats as control volumes and also considering geometry updates due to heterogeneous chemical reaction at each time step of the simulations.

The final and more complex algorithm follows the steps described below:

1. Network construction and geometry data definition.
2. Fluid and solid properties definition.
3. Definition of flow and kinetic parameters.
4. Solution of the steady-state flow field.
5. Definition of initial and boundary conditions, as well as simulation time and time-steps, for the concentration field solution.
6. Set up the sparse linear system of equations constructed based on the pores and throats mass balances using the Euler Implicit Method.
7. Solution of the sparse linear system.
8. After each time step, with the new acid mass concentration (c_A^{n+1})multiplied by the volume (V^n) for each pore and throat, the total mass of acid (m_A) inside each pore and throat is determined.
9. Determination of consumed mass of acid using Eq. (13).
10. Determination of consumed mass of solid using Eq. (14).
11. Determination of consumed volume of solid using Eq. (15).
12. Update the pore-space volume (V^{n+1}) adding the consumed volume (V_{con}) to the previous volume (V^n).
13. Geometry update:
    (a) Determination of the new pore and throat volumes using, respectively, Eqs. (20) and (21).
    (b) Determination of the new pore radii using Eq. (22).
    (c) Determination of the new throat lengths using Eq. (23).
    (d) Determination of the new throat radii using Eq. (24).
    (e) Determination of the new available reactive area and cross-sectional area of throats by using, respectively, Eqs. (25) and (26).
    (f) Determination of the new available reactive area for pores using Eq. (28).
14. Update the hydraulic conductance, Eq. (3), considering the updated geometry.
15. Update the fluid flow field, Eq. (1), considering the updated geometry.
16. Update the new acid mass concentration (c_A^{n+1}) for each pore space considering the total mass of this chemical species inside each pore and throat (m_A) divided by the respective updated volume (V^{n+1}).
17. Return to step 6 and repeat until the algorithm reaches the final time step.

5. Results and discussion

Simulations of reactive transport are performed in different cubic networks to investigate dissolution regimes. The geometry of the simulation domains are based on the work of Song et al. (2014), who conducted dissolution experiments in a real rock micro-model directly etched in to a block of calcite, and of Soulaine et al. (2017), that conducted simulations of the dissolution process in a two-dimensional domain using a micro-continuum DBS approach. In this way, the networks used in this work consider a uniform distribution of the pore sizes, ranging from 300 μm to 900 μm.

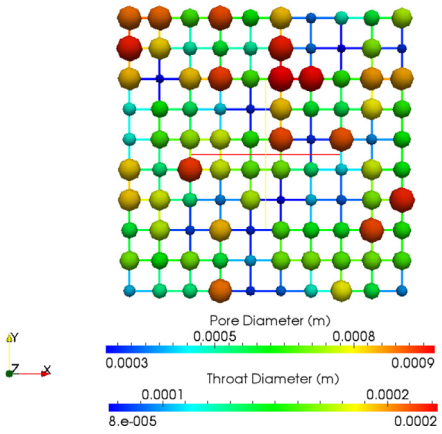

Fig. 1. Pore and throat sizes of the cubic network composed of 10 × 10 pores.

A concentration of $10\,kg/m^3$ of acid is injected from the left-hand side of the network (one-dimensional flow in the positive x direction) at a constant volumetric flow rate corresponding to a $Re \approx 0.1$. Fluid and solid properties are set to $\mu_f = 10^{-3}\ Pa.s$, $\rho_f = 1000\,kg/m^3$ and $\rho_{solid} = 2165\,kg/m^3$. The stoichiometric coefficient that relates the consumed acid species with the consumed solid reactive mineral is set to $\beta = 1$. All these properties are based on the work of Soulaine et al. (2017).

Simulations considered a range in *Pe* from 10^{-3} to 10^2 whereas the *Da* varied from 10^{-3} to 1. In order to obtain these wide ranges of dimensionless numbers, we considered diffusivity coefficients from 10^{-9} to as large as $10^{-4}\ m^2 s^{-1}$ and reaction rate constants from 10^{-6} to $10^{-3}\ m\ s^{-1}$. Alternately, v_0 could have been varied to obtain the desired range of *Pe* and *Da*.

The final simulation time was set to 500 seconds and the time step size was fixed at 1 second. It is important to notice that simulations at the surface regime present a smaller simulation time, due to the limitation of the merging of pores and throats, not yet implemented in this work. Also, Damköhler values are limited to avoid reactivity scenarios where the merging of pore spaces could happen. Likewise, greater reactivity might lead to the formation of a CO_2 phase due to the large amount of reaction product produced. Both of these are topics to be developed in future work. Importantly, the reactivities tested were sufficient to present behaviors of transport-limited processes. The results are discussed based on the pore volumes of injectant (PVI).

Additionally, the last section presents extra simulations considering the carbonate network, including a comparison between our results and those available in the literature.

5.1. Identification of dissolution regimes

A network composed of 10 × 10 pores is used to explore the different dissolution regimes and to construct phase diagrams based on the dimensionless numbers *Pe, Da* and *PeDa*. Fig. 1 presents a scheme of the 10 × 10 network geometry. The simulation results show that, depending on the flow conditions and the mineral reactivity, different geometries and acid distributions can be observed after the dissolution process. These observations agree with previous literature (Daccord et al., 1993b; Golfier et al., 2002; Soulaine et al., 2017; Liu and Mostaghimi, 2017). Three main dissolution patterns and two intermediate patterns are observed from reactive transport simulations: uniform dissolution, surface dissolution, preferential pathways, transition zone, and mixed zone.

The uniform dissolution pattern is related to significant acid penetration in the network. In this regime, the acid consumption rate is

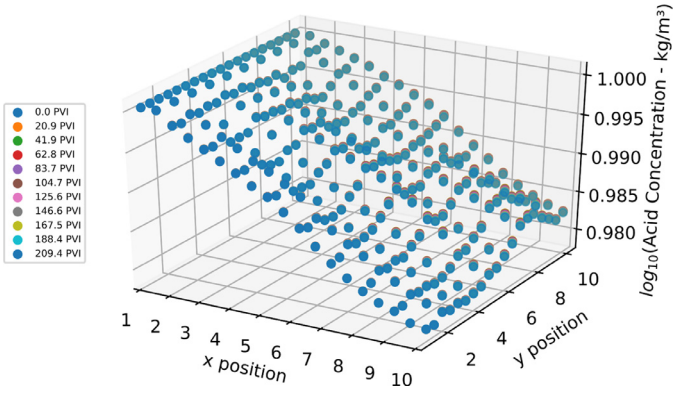

Fig. 2. Evolution of the acid concentration as a function of PVI for pores and throats considering their x and y positions in the 10×10 network in the uniform dissolution I regime ($Pe = 0.00094$ and $Da = 0.00094$).

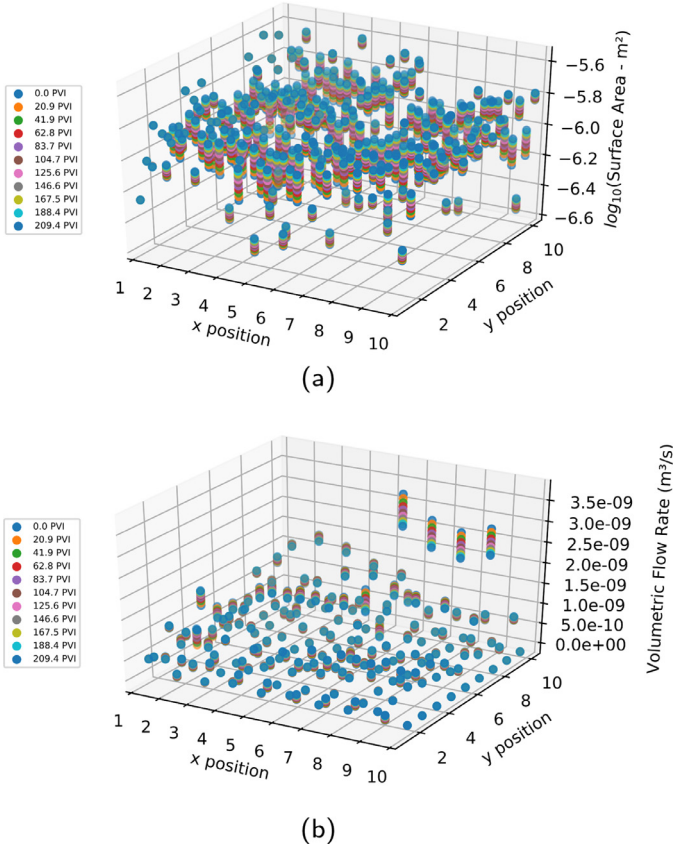

Fig. 3. Simulation results from uniform dissolution II regime ($Pe = 0.00094$ and $Da = 0.0094$): (a) Evolution of the surface area as a function of PVI for pores and throats considering their x and y positions in the 10×10 network; and (b) Evolution of the volumetric flow rate as a function of PVI for throats considering their x and y positions in the 10×10 network.

smaller than the transport by diffusion and advection, meaning that almost the entire pore space is filled with a uniform distribution of the acid (see Fig. 2). When a sufficiently large reactivity exists, the changes in pore-space geometry happen throughout the entire domain (see Fig. 3a). Otherwise, no significant changes are observed throughout the network. This is a consequence of the availability of acid for all pore spaces of the network, that characterizes the reaction-limited feature of this dissolution regime. The volumetric flow rate starts to present changes for a $Da \approx 0.01$, that are more evident for throats with larger permeability (see Fig. 3b). The standard deviation based on acid concentration data

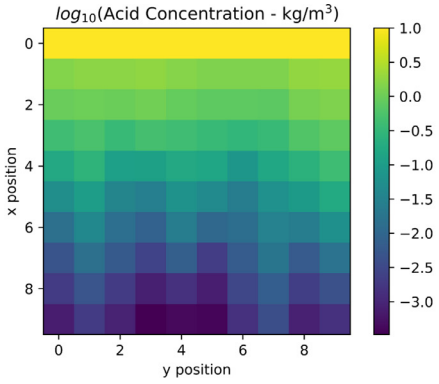

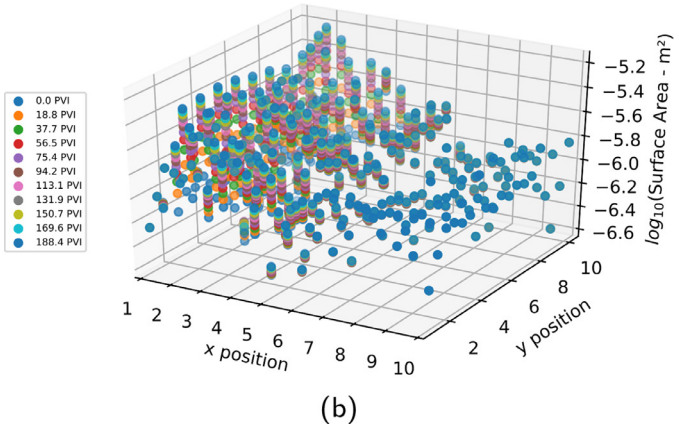

Fig. 4. Simulation results from surface dissolution regime ($Pe = 0.00094$ and $Da = 0.47$): (a) Final acid concentration profile (flow is from the top to the bottom); and (b) Evolution of the surface area as a function of PVI for pores and throats considering their x and y positions in the 10×10 network.

from all pore spaces, σ_{net}, was determined for 100 networks and for 100% of the samples presented a value less than one, evidencing the uniform pattern of the regime.

The transition zone is characterized by the decrease of the acid penetration through the network and a concentration of the geometry changes in some portions of the domain. Regardless of the Péclet number in this Da range, this behavior is observed.

The surface dissolution pattern is characterized by a homogeneous acid concentration along the cross-sections perpendicular to the flow (see Fig. 4a). In this regime, the diffusion mechanism dominates over advective transport and reactivity of the acid is high, meaning that significant amounts of acid are consumed on the upstream pore spaces of the network thereby impairing the propagation of the acid through the entire porous medium. Because of this, the largest changes in geometry are observed for pores and throats located near the inlet area of the network (see Fig. 4b). The standard deviation analysis was evaluated and presented $\sigma_{net} > 1$ and $\overline{\sigma_{cross}} < 1$ for 100% of the samples. This confirms the uniform profile of acid concentration along cross-sections perpendicular to the flow.

The mixed zone is characterized as a transition between surface dissolution and preferential pathways. In this regime, the homogeneity of acid concentration along vertical cross-sections starts to disappear, as well as other features of surface regime.

The preferential pathways are observed when advection is the strongest transport mechanism and the reactivity of the acid is high. Preferential pathways result from the heterogeneous geometry of the porous medium and consequent heterogeneous velocity profile. Because

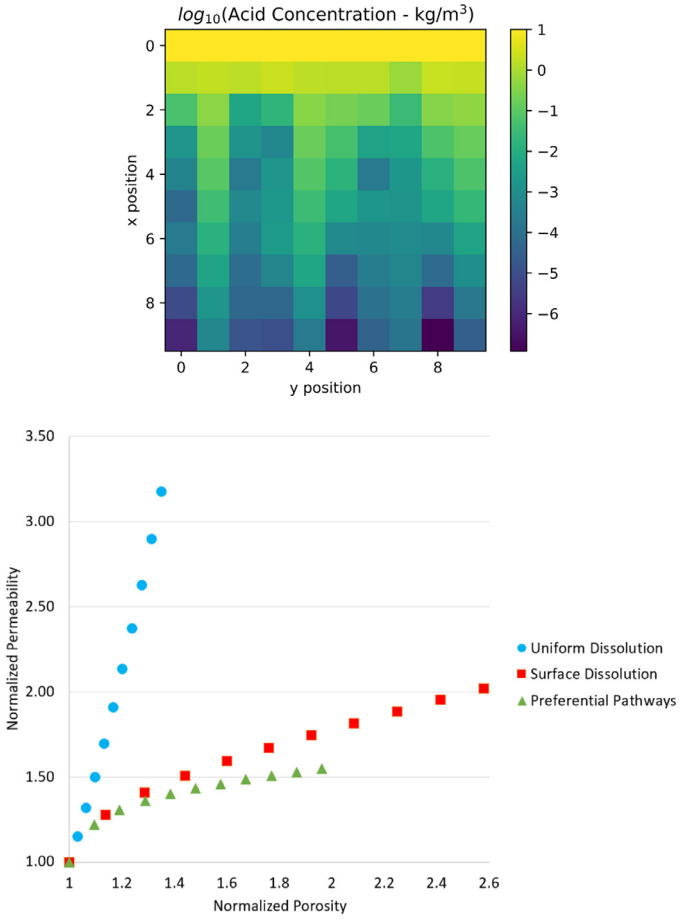

Fig. 6. Evolution of the porosity-permeability relationship results from 10 × 10 network simulations.

of this, more acid penetrates into the network through the more permeable pathways and no uniform patterns are observed (see Fig. 5). Furthermore, geometry changes in this regime are also more evident along the most permeable areas, as well as changes in volumetric flow rates. The standard deviation analysis presented $\sigma_{net} > 1$ for 100% of the samples and $\overline{\sigma_{cross}} > 1$ for 96% of the samples, evidencing the formation of preferential pathways through the domain.

Fig. 6 presents the evolution of the relationship between normalized permeability and porosity for the three main dissolution regimes observed. For the uniform dissolution, a linear pattern is observed, independent of the mineral reactivity considered. This means that, besides the increase in porosity, absolute permeability of the porous medium also increases as a consequence of geometry changes in the entire network. A power law pattern is observed for the surface dissolution regime that can be interpreted as a restriction caused by the transport. Even with an increase of the porosity, the overall permeability does not increase at the same rate because the majority of the affected pores are in the inlet. A similar pattern is observed for preferential pathways, however with a smaller increase of the porosity when compared to the surface dissolution.

The difference in the increase of permeability for preferential pathways and surface dissolution regimes is explained by the extent of acid contact with solid throughout the entire network volume. After 209.4 PVI of injection, the pore spaces that have undergone dissolution by the presence of acid in the preferential pathways regime are less in volume than those affected in the surface dissolution regime (188.4 PVI), and also the uniform dissolution regime (209.4 PVI). That is, the fraction of the pore volume of the network that is affected by dissolution in the preferential pathways regime is less than the other two regimes and pathways do not span the sample. Fig. 5, for example, is an image of the final acid concentration distribution in the preferential pathway regime. Note that the pathways do not span from the injection side to the production side.

5.2. Behavior diagram construction

In order to summarize the different dissolution regimes observed in the reactive transport simulations conducted on the network composed by 10 × 10 pores, behavior diagrams are constructed based on the *Pe, Da* and *PeDa* dimensionless numbers, as presented in Figs. 7a and 7b. The main features of the diagrams agree well with literature results, especially when compared with the study of Soulaine et al. (2017) that presents a regime diagram based on *Pe* and *Da*, and the work of Golfier et al. (2002) that present the regime diagrams based on *Pe, Da* and *PeDa*. Considering that the transition boundaries are based mostly on qualitative observation, some uncertainties are associated with these lines and discrepancies between the studies can be noticed. The pore network modeling used in this study is not capable yet to explore different preferential pathways regimes, as by previous studies did (Golfier et al., 2002; Soulaine et al., 2017); However, the main dissolution regimes are explored by using a different analysis tool, as presented in this section. Furthermore, because this model does not consider merging of pores and throats, this limitation also may bring some difference in the analysis of the boundaries and regimes. It is also important to remember that dimensionless numbers are computed differently in each of the literature studies and this may explain these discrepancies. After all, it is important to highlight the applicability of pore network modeling as a tool to investigate dissolution regimes.

Concerning length scale effects, a network composed of 10 × 40 pores is used to investigate possible differences in the construction of behavior diagrams of different network sizes. From Fig. 8 , it is possible to note that, besides all the agreements compared to the results from 10 × 10 network, a small discrepancy related to the mixed zone is observed. The transition pattern between surface dissolution and preferential pathways is reduced for the 10 × 40 network and is related to the increase of network heterogeneity, and consequently a faster transition between regimes with large mineral reactivity. Therefore, regardless of the difference in the mixed zone, one can conclude that the behavior diagrams are in good agreement considering networks with different sizes.

5.3. Verification in a 40 × 40 network

Considering here, a network with 40 × 40 pores, the main dissolution regimes are verified. Fig. 9 presents the acid concentration profile for uniform, surface dissolution, and preferential pathways regimes, respectively, after 50.6 PVI, 40.5 PVI and 50.6 PVI (Figs. 9a–c). The behaviors observed agree with the discussed features of each of the regimes: uniform dissolution presents a uniform concentration of acid through the entire domain, surface dissolution is characterized by a homogeneous concentration profile along the cross-sections perpendicular to the flow and preferential pathways area highlighted by acid distribution through most permeable areas. Additionally, Fig. 10 presents the porosity-permeability relationship of these regimes. The linear pattern of the uniform distribution is apparent as well as the power law pattern of surface dissolution and preferential pathways. It is important to observe here that surface dissolution again presents greater increase of porosity than preferential pathways due to the large dissolution rate for inlet pore spaces, even with the lack of pore merging. The importance of surface dissolution is also evidence of the role of diffusion. The standard deviations of these simulations were obtained and also agree with the regime specifications.

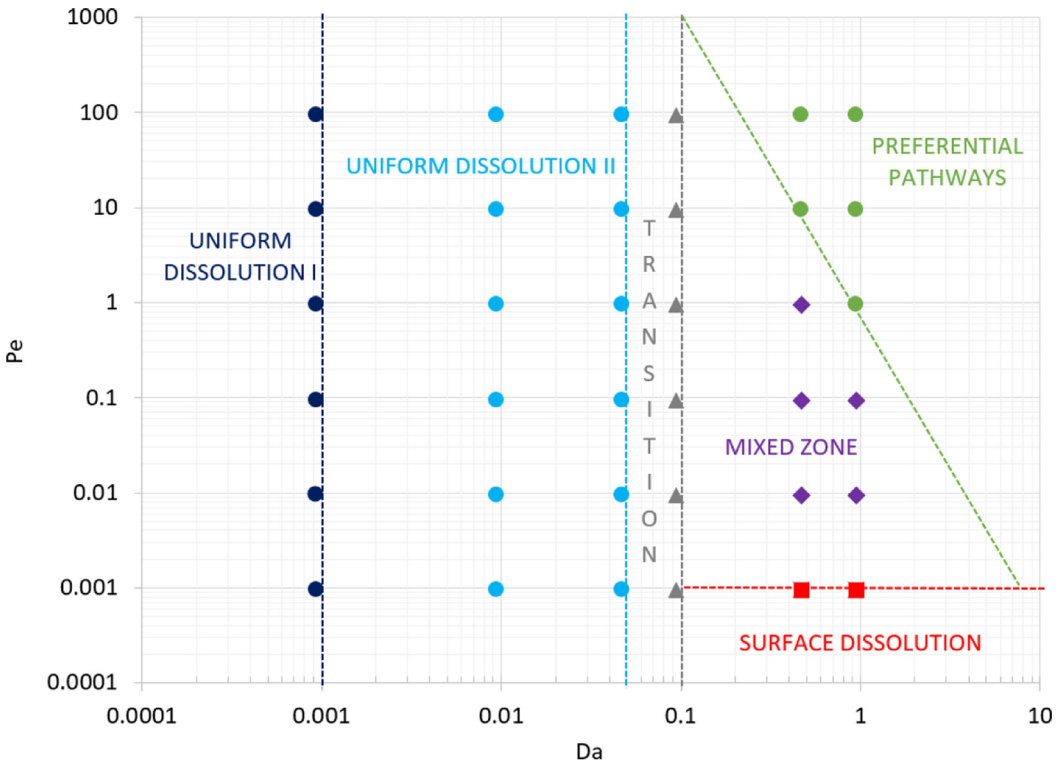

(a)

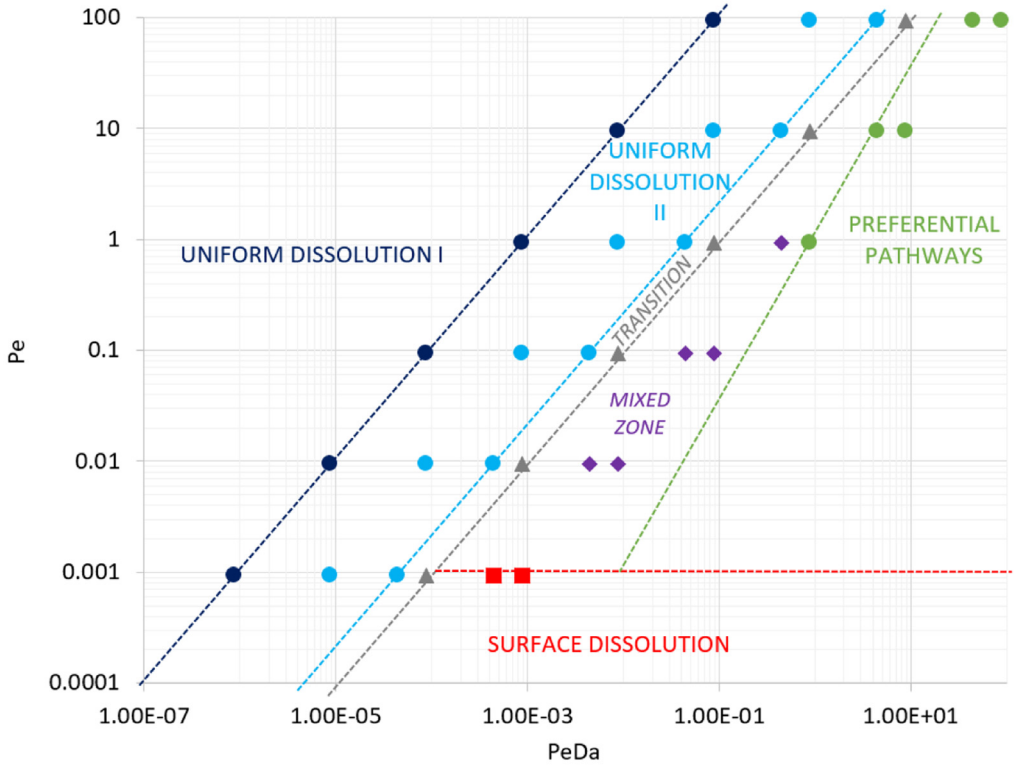

(b)

Fig. 7. Behavior diagrams constructed from 10 × 10 network simulations: (a) Pe-Da; and (b) Pe-PeDa.

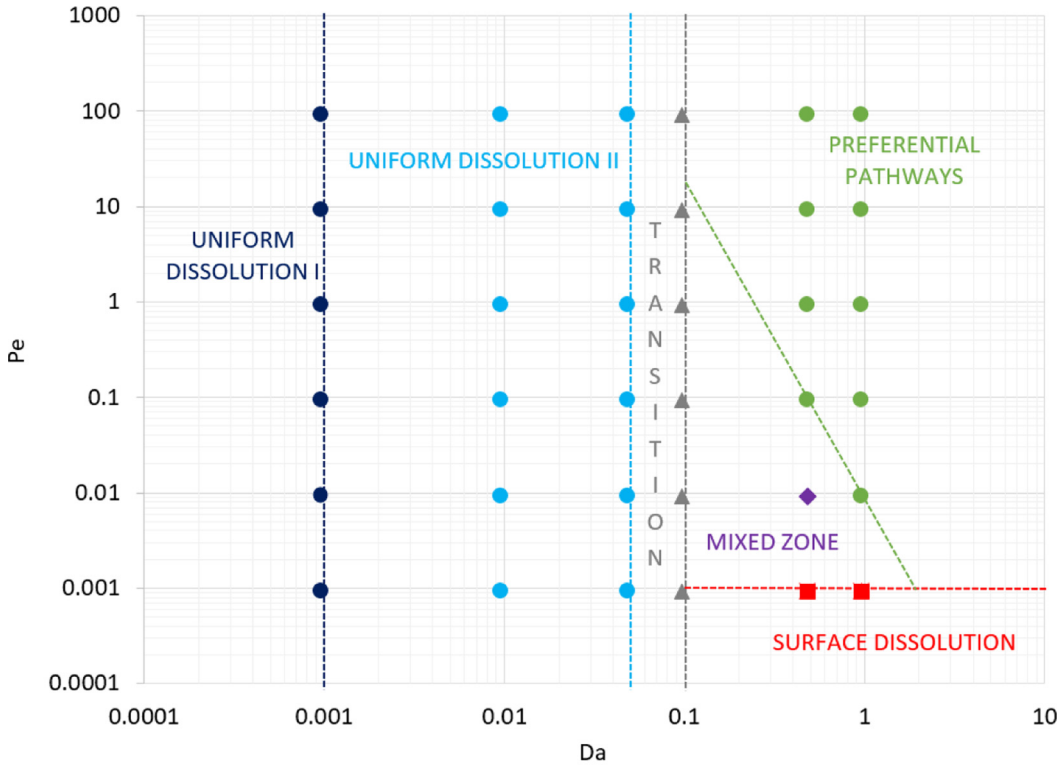

(a)

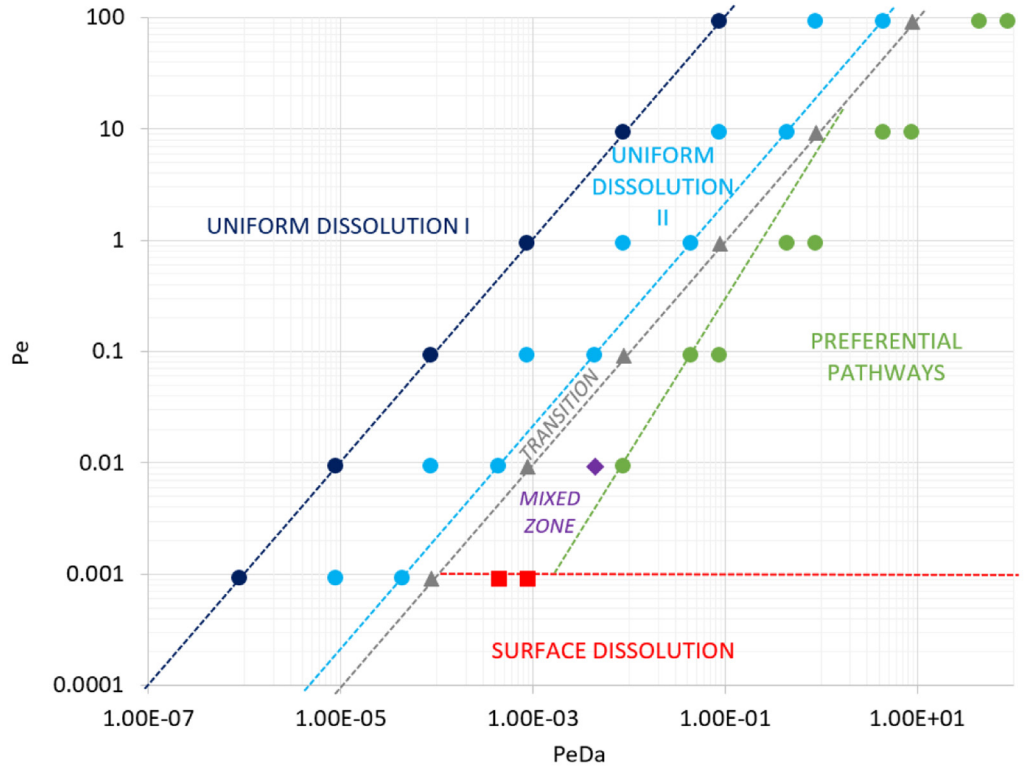

(b)

Fig. 8. Behavior diagrams constructed from 10 × 40 network simulations: (a) Pe-Da; and (b) Pe-PeDa.

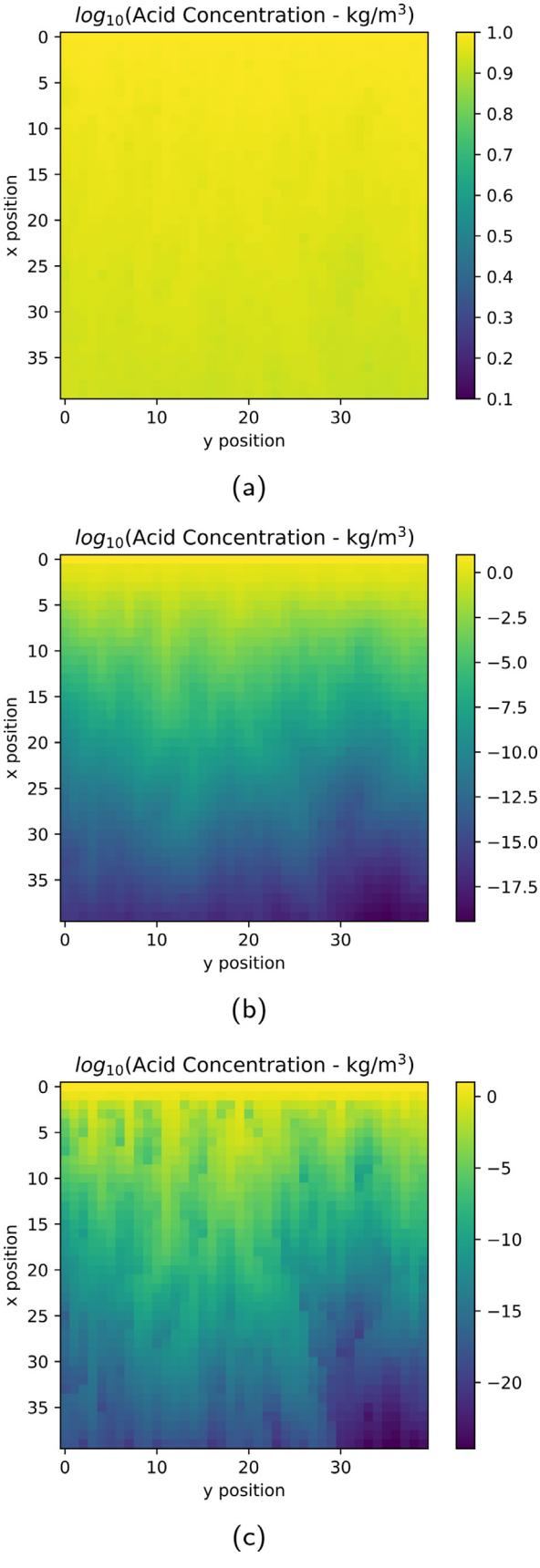

Fig. 9. Final acid concentration profile in the 40 × 40 network (flow is from the top to the bottom): (a) Uniform dissolution ($Pe = 0.094$ and $Da = 0.0007$); (b) Surface dissolution ($Pe = 0.00094$ and $Da = 0.45$); and (c) Preferential pathways ($Pe = 94$ and $Da = 0.45$). Note that the color scale is different for each subfigure to feature differences among the regimes.

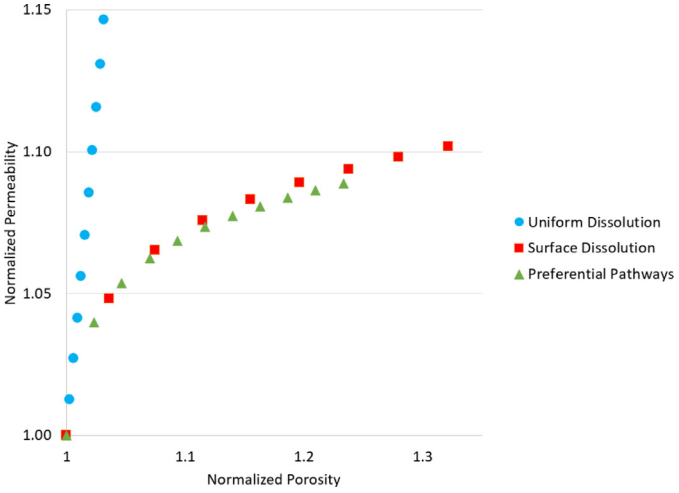

Fig. 10. Porosity-permeability relationship results from 40 × 40 network simulations.

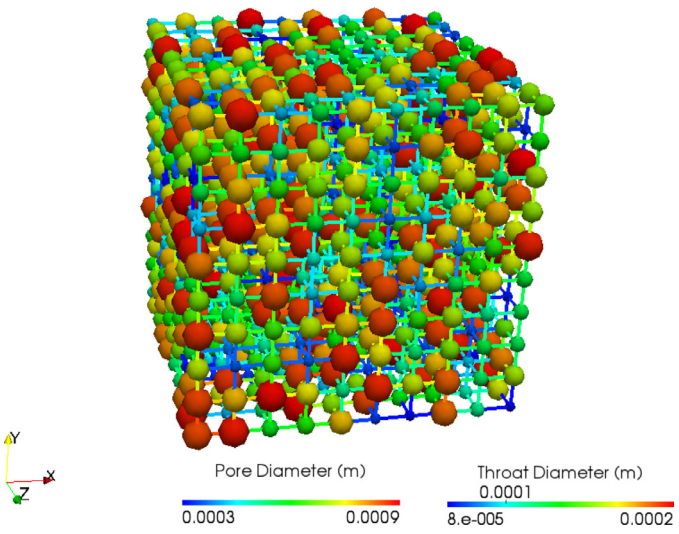

Fig. 11. Scheme of the initial geometry for the network composed of 10 × 10 × 10 pores.

5.4. 3D domain verification

A three dimensional domain is constructed to evaluate the generality of the features of the dissolution regimes obtained using 2D pore networks. Fig. 11 presents the initial geometry for a network composed by 10 × 10 × 10 pores.

The acid concentration for uniform dissolution, surface dissolution and preferential pathways after 250.2 PVI, 150.1 PVI and 250.2 PVI, respectively, are presented in Fig. 12. The features of each regime agree with discussions made considering 2D networks. The uniform dissolution (see Fig. 12a) presents a uniform distribution of the acid throughout the entire domain and shows a $\sigma_{net} = 0.01$ for the conditions assumed ($Pe = 0.095$, $Da = 0.0006$ and $PeDa = 6.06 \times 10^{-5}$). The surface dissolution (see Fig. 12b) presents a homogeneous distribution of the acid concentration along cross-sections perpendicular to the flow. The standard deviations of this regime and the dimensionless numbers result, respectively, in $\sigma_{net} = 1.56$ and $\overline{\sigma_{cross}} = 0.39$, and $Pe = 0.00095$, $Da = 0.57$ and $PeDa = 5.456 \times 10^{-4}$, that agree with the previous assumptions. The preferential pathways (see Fig. 12c) are well observed in the middle region of the network considering $Pe = 95$, $Da = 0.57$ and $PeDa =$

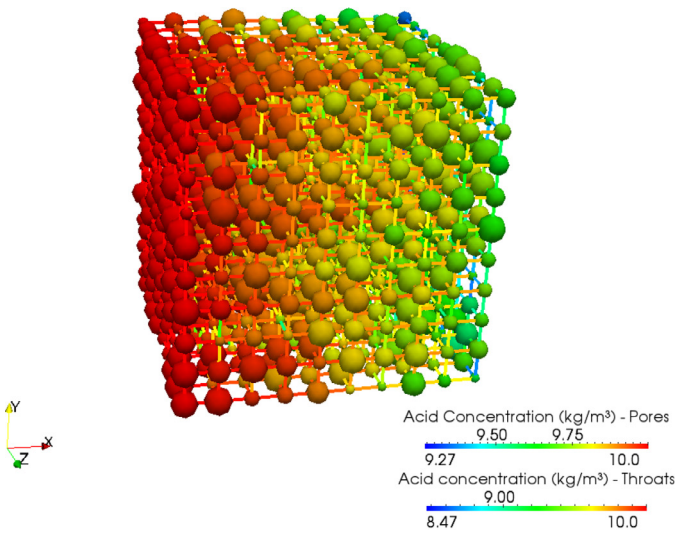

(a)

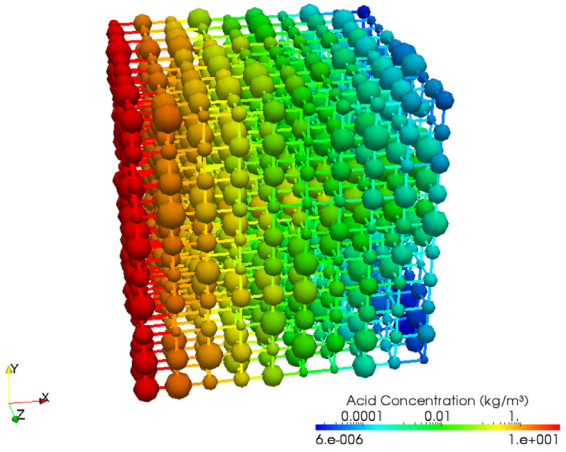

(b)

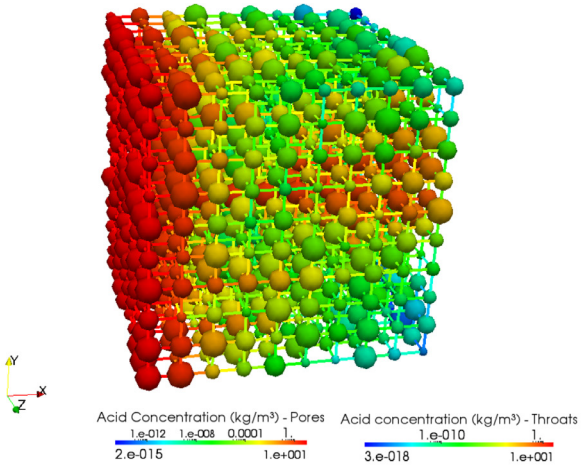

(c)

Fig. 12. Acid concentration for the network composed by $10 \times 10 \times 10$ pores: (a) Uniform Dissolution; (b) Surface Dissolution; and (c) Preferential Pathways.

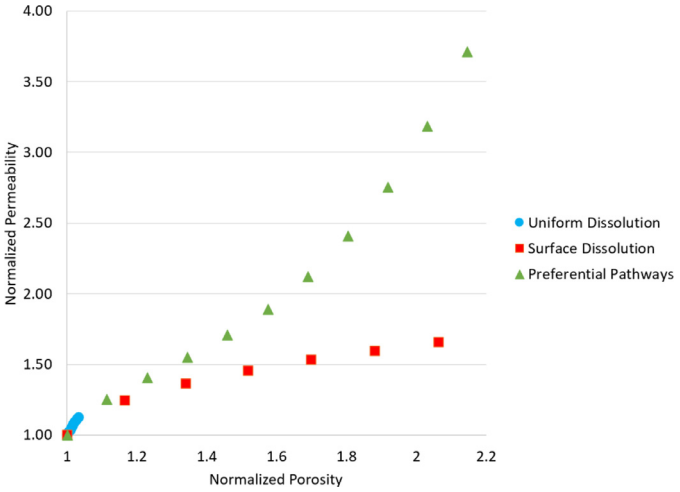

Fig. 13. Porosity-permeability relationship results from $10 \times 10 \times 10$ network simulations.

5.456×10^1. The standard deviation of this condition is $\sigma_{net} = 3.52$ and $\overline{\sigma_{cross}} = 2.31$.

The porosity-permeability relationships for the three main dissolution regimes are presented in Fig. 13. The uniform dissolution regime presents a linear pattern, as observed for 2D simulations. The surface dissolution result also replicates the results obtained for 2D domains, that present a more rapid increase of the porosity in comparison to the permeability as a result of the geometry changes in the inlet area of the networks. On the other hand, the preferential pathways presents a slightly different pattern, where a power-law behavior is observed initially (at normalized porosity range of $1 - 1.2$), followed by a pronounced increase of the permeability, that characterizes the formation of preferential pathways. This difference is related to the greater degree of freedom for 3D simulations that allows more propagation options for the fluid throughout the porous medium and increases the evidence of highly conductive channels formation. These different behaviors in 2D and 3D networks are expected, because the preferential pathways regime tends to create fractal structures (Daccord et al., 1987; 1993a) that depend on the dimensionality of the enclosing domain.

5.5. Implementation on real pore networks

The single-phase reactive transport approach developed in this work was also implemented using a pore network obtained from a carbonate rock. This pore network model is used to ensure the applicability of this methodology for more complex pore topologies. Here, the inlet acid concentration is set to $1\,kg/m^3$ and a reaction-limited scenario is presented, considering $Da = 0.001$. Greater reactivities cannot be considered without including the merging of pores and throats.

Fig. 14 presents the final concentration profile of a uniform dissolution pattern simulation, that is in good agreement with the behaviors observed in cubic networks and presenting $\sigma_{net} = 0.003$.

The results of porosity and permeability evolution from these simulations are compared with regular cubic network results and literature data. The power-law exponent of the curves obtained by plotting $log(K/K_0)$ versus $log(\phi/\phi_0)$ are compared with values obtained by Egermann et al. (2010) and Bekri et al. (2015). Both worked with 3D regular pore networks constructed based on petrophysical laboratory data. Egermann et al. (2010) also conducted core-flood experiments. The latter, related the power-law exponent with the dissolution pattern, where reaction-limited regimes were identified between values of 1.5 and 6.9 (identified in Table 1 by the subscripts *min* and *max*, respectively). Greater values were related to a convective-predominant regime

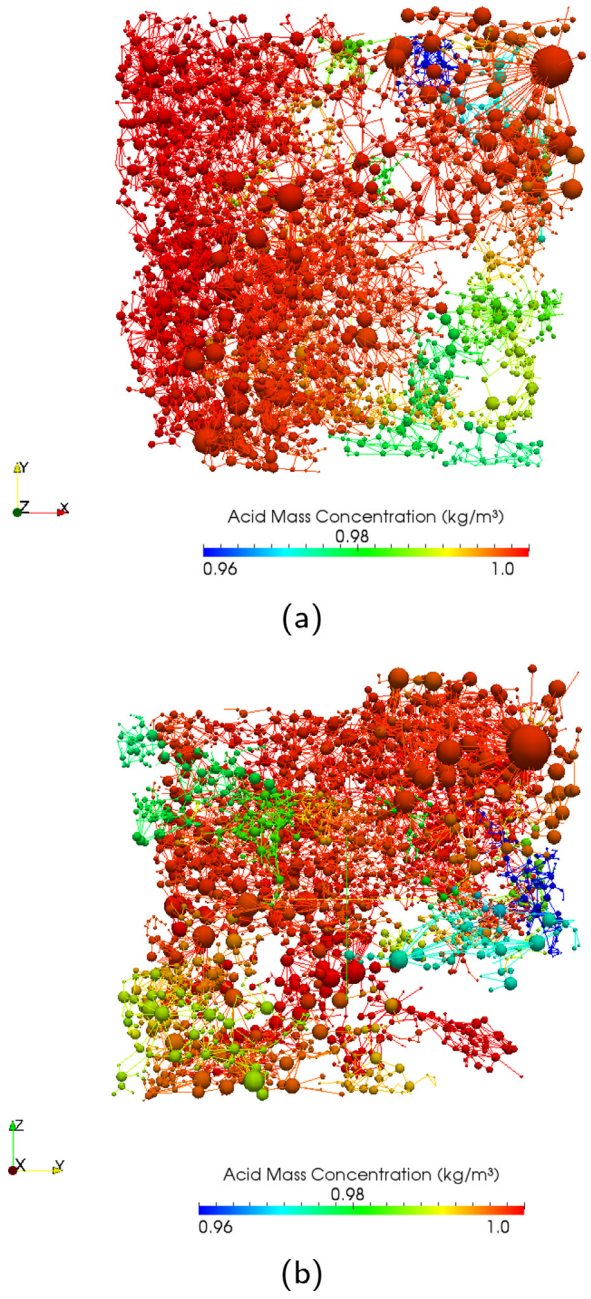

Fig. 14. Final acid concentration profile for a uniform dissolution regime simulation in network derived from a carbonate rock sample with views at different angles (a and b). A narrow concentration scale is used to highlight the differences in concentration within the network.

Table 1
Comparison among power-law exponents for the uniform dissolution regime.

Reference	Slope
Egermann et al. (2010)$_{throats}$	31.0
Carbonate	24.3
Egermann et al. (2010)$_{max}$	6.9
2D Regular Network (10 × 10)	4.0
3D Regular Network (10 × 10 × 10)	3.7
Bekri et al. (2015)	3.2
Egermann et al. (2010)$_{min}$	1.7

described by changes only in throats geometry (value identified by the subscript *throats*).

Table 1 presents the power-law exponents and their references. It is noticed that simulations in the 2D and 3D pore networks previously discussed in this work, and from Bekri et al. (2015) obtained values in the range that represents uniform dissolution. For the carbonate simulation, the exponent is larger and is explained by the fact that the available surface areas obtained for this sample (see Eq. (28)) are much smaller due to the significant heterogeneity of the pore and throat sizes. Consequently, for this case, changes were observed mainly in the permeability due to dissolution of throats.

As for future work, the implementation of merging of pores and throats would improve and facilitate the use of the approach presented in this study to evaluate dissolution regimes in more complex pore networks derived from real porous media. This will likely change the response of permeability and porosity for extreme cases, respectively represented by preferential pathways and surface dissolution regimes, and also bring the reactive transport model to the physical problem.

6. Conclusion

This work presents a pore-network modeling approach to evaluate the effects of different transport mechanisms and mineral reactivity on dissolution regimes, as well as changes in porosity and permeability. The transport problem is implemented by considering the acid mass balance inside pores and throats. The changes in pore-space geometry due to dissolution are considered based on the rate of the heterogeneous chemical reaction happening at the solid surface. Péclet and Damköhler dimensionless numbers are used to construct behavior diagrams in order to characterize the different dissolution regimes.

The reactive transport simulations developed in this work exhibit results similar to those previously discussed in the literature based on direct simulations and experimental trials. In this work, five dissolution regimes were explored based on acid concentration, network geometry, volumetric flow rate, porosity-permeability relationship, and standard deviation analysis, that was successfully introduced as a quantitative criterion for the cases studied. These regimes include uniform dissolution ($Da < 0.05$), transition zone ($0.05 < Da < 0.1$), surface dissolution ($Da > 0.1$ and $Pe < 0.001$), mixed zone, and preferential pathways (in general, for $Da > 0.1$ and $Pe > 0.001$).

The results demonstrate the applicability of pore-network modeling as a tool to explore reactive transport and dissolution processes, as well as to predict changes in porosity and permeability. Results demonstrated the various dissolution regimes observed at larger scales. The use of a pore-network approach to understand reactive transport during single-phase flow also offers new possibilities of investigation.

Merging of pores and throats to form vug-like pores is suggested as an improvement to better evaluate regimes with significant mineral reactivity. Incorporation of cornered pores with triangular geometry, that are the most common pore shape, allows the exploration of more complex systems based on multiphase reactive transport. In this way, multiphase systems are also suggested to be implemented to represent various subsurface and reservoir conditions.

Declaration of Competing Interest

The authors declare that they have no known competing financial interests or personal relationships that could have appeared to influence the work reported in this paper.

CRediT authorship contribution statement

Barbara F. Esteves: Conceptualization, Methodology, Software, Writing - original draft. **Paulo L.C. Lage:** Writing - review & editing, Supervision. **Paulo Couto:** Writing - review & editing, Supervision.

Anthony R. Kovscek: Conceptualization, Supervision, Funding acquisition, Writing - review & editing.

Acknowledgment

BFE and ARK acknowledge gratefully the support of the Stanford Center for Carbon Storage.

Supplementary material

Supplementary material associated with this article can be found, in the online version, at 10.1016/j.advwatres.2020.103741

References

Algive, L., Bekri, S., Robin, M., Vizika, O., 2007. Reactive transport: experiments and pore-Network modelling. Int. Symp. Soc. Core Anal. (1969) 1–13.

Algive, L., Bekri, S., Vizika, O., 2010. Pore-network modeling dedicated to the determination of the petrophysical-Property changes in the presence of reactive fluid. SPE J. 15 (03), 618–633. https://doi.org/10.2118/124305-PA.

Bekri, S., Renard, S., Delprat-Jannaud, F., 2015. Pore to core scale simulation of the mass transfer with mineral reaction in porous media. Oil Gas Sci. Technol. Revue d'IFP Energies nouvelles 70 (4), 681–693. https://doi.org/10.2516/ogst/2014046.

Békri, S., Thovert, J.F., Adler, P.M., 1995. Dissolution of porous media. Chem. Eng. Sci. 50 (17), 2765–2791. https://doi.org/10.1016/0009-2509(95)00121-K.

Bemer, E., Lombard, J.M., 2010. From injectivity to integrity studies of co_2 geological storage. Oil Gas Sci. Technol. 65 (3), 445–459. https://doi.org/10.2516/ogst/2009028.

Bird, R., Steward, W., Lightfoot, E., 2011. Fenomenos de Transporte. LTC, Rio de Janeiro.

Daccord, G., Lenormand, R., Liétard, O., 1987. Fractal patterns from chemical dissolution. Nature 325, 41–43. https://doi.org/10.1038/325041a0.

Daccord, G., Lenormand, R., Liétard, O., 1993. Chemical dissolution of a porous medium by a reactive fluid-I. Model for the "wormholing" phenomenon. Chem. Eng. Sci. 48 (1), 169–178. https://doi.org/10.1016/0009-2509(93)80293-Y.

Daccord, G., Liétard, O., Lenormand, R., 1993. Chemical dissolution of a porous medium by a reactive fluid-II. Convection vs reaction, behavior diagram. Chem. Eng. Sci. 48 (1), 179–186. https://doi.org/10.1016/0009-2509(93)80294-Z.

Egermann, P., Bekri, S., Vizika, O., 2010. An integrated approach to assess the petrophysical properties of rocks altered by rock-fluid interactions (CO_2injection). Petrophysics 51 (1), 32–40.

Fatt, I., 1956. The network model of porous media. Pet. Trans., AIME 207, 144–181.

Fredd, C.N., Dowell, S., 2000. Advances in Understanding and Predicting Wormhole Formation, 3 Wiley.

Fredd, C.N., Fogler, H., 1998. Influence of transport and reaction on wormhole formation in porous media. AlChE J. 44 (9), 1933–1949. https://doi.org/10.1002/aic.690440902.

Fredd, C.N., Fogler, H., 1999. Optimum conditions for wormhole formation in carbonate porous media: influence of transport and reaction. SPE J. 4 (03). https://doi.org/10.2118/56995-PA.

Gharbi, O., Bijeljic, B., Boek, E., Blunt, M.J., 2013. Changes in pore structure and connectivity induced by CO_2 injection in carbonates: a combined pore-scale approach. Energy Procedia 37 (0), 5367–5378. https://doi.org/10.1016/j.egypro.2013.06.455.

Golfier, F., Zarcone, C., Bazin, B., Lenormand, R., Lasseux, D., Quintard, M., 2002. On the ability of a Darcy-scale model to capture wormhole formation during the dissolution of a porous medium. J. Fluid Mech. 457, 213–254. https://doi.org/10.1017/S0022112002007735.

Gostick, J., Aghighi, M., Hinebaugh, J., Tranter, T., Hoeh, M.A., Day, H., Spellacy, B., Sharqawy, M.H., Bazylak, A., Burns, A., Lehnert, W., Putz, A., 2016. Openpnm: a pore network modeling package. Comput. Sci. Eng. 18 (4), 60–74.

Hill, a.D., Schechter, R.S., 2000. Fundamentals of Acid Stimulation, 3 Wiley.

Hoefner, M.L., Fogler, H.S., 1988. Pore evolution and channel formation during flow and reaction in porous media. AlChE J. 34 (1), 45–54. https://doi.org/10.1002/aic.690340107.

Jones, E., Oliphant, T., Peterson, P., et al., 2001. SciPy: Open source scientific tools for Python. Acessed: 2020-05-05.

Li, L., Peters, C.A., Celia, M.A., 2006. Upscaling geochemical reaction rates using pore-scale network modeling. Adv. Water Resour. 29 (9), 1351–1370. https://doi.org/10.1016/j.advwatres.2005.10.011.

Liu, M., Mostaghimi, P., 2017. Characterisation of reactive transport in pore-scale correlated porous media. Chem. Eng. Sci. 173, 121–130. https://doi.org/10.1016/j.ces.2017.06.044.

Mehmani, Y., Balhoff, M.T., 2015. Mesoscale and hybrid models of fluid flow and solute transport. Rev. Mineral. Geochem. 80 (1), 433–459. https://doi.org/10.2138/rmg.2015.80.13.

Menke, H.P., Reynolds, C.A., Andrew, M.G., Pereira Nunes, J.P., Bijeljic, B., Blunt, M.J., 2018. 4D Multi-scale imaging of reactive flow in carbonates: assessing the impact of heterogeneity on dissolution regimes using streamlines at multiple length scales. Chem. Geol. 481 (January), 27–37. https://doi.org/10.1016/j.chemgeo.2018.01.016.

Ott, H., Oedai, S., 2015. Wormhole formation and compact dissolution in single- and two-phase CO_2-brine injections. Geophys Res Lett 42 (7), 2270–2276. https://doi.org/10.1002/2015GL063582.

PERM - Petroleum Engineering & Rock Mechanics Group,. Imperial College London - PERM - Pore-Scale Modelling and Imaging.Acessed: 2020-04-13.

Raoof, A., Nick, H.M., Wolterbeek, T.K., Spiers, C.J., 2012. Pore-scale modeling of reactive transport in wellbore cement under CO_2 storage conditions. Int. J. Greenhouse Gas Control 11 (SUPPL), 67–77. https://doi.org/10.1016/j.ijggc.2012.09.012.

Rathnaweera, T.D., Ranjith, P.G., Perera, M.S., 2016. Experimental investigation of geochemical and mineralogical effects of CO_2 sequestration on flow characteristics of reservoir rock in deep saline aquifers. Sci. Rep. 6 (September 2015), 1–12. https://doi.org/10.1038/srep19362.

Sohrabi, M., Kechut, N.I., Riazi, M., Jamiolahmady, M., Ireland, S., Robertson, G., 2012. Coreflooding studies to investigate the potential of carbonated water injection as an injection strategy for improved oil recovery and CO_2 storage. Transp. Porous Media 91 (1), 101–121. https://doi.org/10.1007/s11242-011-9835-5.

Song, W., De Haas, T.W., Fadaei, H., Sinton, D., 2014. Chip-off-the-old-rock: the study of reservoir-relevant geological processes with real-rock micromodels. Lab Chip 14 (22), 4382–4390. https://doi.org/10.1039/c4lc00608a.

Song, W., Ogunbanwo, F., Steinsbø, M., Fernø, M.A., Kovscek, A.R., 2018. Mechanisms of multiphase reactive flow using biogenically calcite-functionalized micromodels. Lab Chip 18 (24), 3881–3891. https://doi.org/10.1039/C8LC00793D.

Soulaine, C., Roman, S., Kovscek, A., Tchelepi, H.A., 2017. Mineral dissolution and wormholing from a pore-scale perspective. J. Fluid Mech. 827, 457–483. https://doi.org/10.1017/jfm.2017.499.

Steefel, C.I., Mäher, K., 2009. Fluid-rock interaction: a reactive transport approach. Rev. Mineral. Geochem. 70 (1988), 485–532. https://doi.org/10.2138/rmg.2009.70.11.

Tansey, J., Balhoff, M.T., 2016. Pore network modeling of reactive transport and dissolution in porous media. Transp. Porous Media 113 (2), 303–327. https://doi.org/10.1007/s11242-016-0695-x.

Wolterbeek, T.K., Raoof, A., 2018. Meter-Scale reactive transport modeling of CO_2-Rich fluid flow along debonded wellbore casing-Cement interfaces. Environ. Sci. Technol. 52 (6), 3786–3795. https://doi.org/10.1021/acs.est.7b05358.

Yang, X., Mehmani, Y., Perkins, W.A., Pasquali, A., Schönherr, M., Kim, K., Perego, M., Parks, M.L., Trask, N., Balhoff, M.T., Richmond, M.C., Geier, M., Krafczyk, M., Luo, L.S., Tartakovsky, A.M., Scheibe, T.D., 2016. Intercomparison of 3D pore-scale flow and solute transport simulation methods. Adv. Water Resour. 95, 176–189. https://doi.org/10.1016/j.advwatres.2015.09.015.